Check for updates

Layered double hydroxide based composite core–shell electrospun nanofibers for lead and fluoride filtration from contaminated streams†

Manu Sharma,[a] Rushabh Murali,[a] Karthik K.,[b] Keerthi P. [ID][b] and Somak Chatterjee [ID] *[a]

Coaxial electrospinning was used to synthesize polyacrylonitrile–polyethersulfone (PAN–PES) core–shell nanofibers with magnesium–aluminum layered double hydroxide (Mg–Al LDH) for filtration of lead and fluoride from contaminated streams. Fiber geometry was characterized at a 0.5 mL h^{-1} flow rate for the core polymer (PES/LDH) and 0.8 mL h^{-1} flow rate for the shell polymer (PAN), with a potential of 23 kV and a distance of 15–17 cm between the collector and the needle head. A homogeneous fiber shape was achieved using an optimal LDH concentration of 0.7%. The prepared nanofibers served as an ultrafiltration membrane with a permeability of 5×10^{-12} m s^{-1} Pa^{-1}. The uptake capacity of the produced nanofibers for fluoride and lead was estimated to be 948 mg g^{-1} and 196 mg g^{-1}, respectively at 298 K as per Langmuir's isotherm model. These fibers exhibited hydrophilic properties and possessed a significant level of porosity. XPS study revealed binding energies of 139.3 eV and 685.2 eV, indicating lead and fluoride uptake by the nanofibers. Ether, sulfone, hydroxyl and nitrile groups found in the nanofibers' shell and core most likely contributed to the lead and fluoride uptake. This facilitated the uptake of both ions on the surface of the nanofibers. In terms of the inhibition effect, fluoride had a stronger masking effect compared with lead in a multicomponent solution (consisting of lead and fluoride). Dynamic vacuum filtration was also investigated using the prepared nanofibers in artificial and real-life feed solutions.

1. Introduction

Contamination of pollutants in groundwater streams is one of the major concerns in the Indian subcontinent.[1] The persistent and recurring nature of different pollutants renders natural freshwater bodies, such as ponds, lakes, and rivers, unusable for drinking.[2] Apart from soil contamination, these ions additionally leach into aquifers, thereby contaminating groundwater reserves. One such pollutant is fluoride. It is present in magmatic rocks, such as granite, basalt, limestone, dolomite, shale and minerals, such as topaz and quartz.[3] Natural weathering of such rocks accompanied by untreated industrial discharges from petroleum refineries, steel works and fertilizer plants are some of the primary reasons for its contamination. Consumption of water procured from fluoride-laden streams leads to life-threatening diseases, such as fluorosis, osteosarcoma, nerve paralysis, respiratory problems, rare bone tumors, and prostate cancer.[4] Similarly, the heavy metal ion lead is

another dangerous trace pollutant. Unlike fluoride, lead contamination mainly occurs due to anthropogenic causes, including industrial and landfill discharges, plumbing material corrosion, atmospheric deposition and mining.[5] Similar to other persistent pollutant contamination, lead contamination causes neuropathy, gastrointestinal cancers, mutation in infants, deficits in reaction time, hand-eye coordination defects, fine motor function disruption, convulsions and coma.[6]

The World Health Organization (WHO) and other international regulatory bodies have established stringent guidelines to limit the fluoride and lead concentrations in drinking water, recognizing their potential hazard at lower levels. For example, allowable concentrations of fluoride and lead in potable water are 1.5 mg L^{-1} and 10 μg L^{-1}, respectively.[7] A combined multidisciplinary approach involving materials science, surface chemistry and chemical engineering is required to achieve this. Different scientific techniques have been developed to address this issue, ranging from coagulation,[8] membrane filtration,[9] adsorption,[10] electrodialysis,[11] to ion exchange,[12] to arrest the same.

However, some traditional water treatment methods such as precipitation, adsorption and ion exchange often struggle to remove pollutants at low concentrations.[13] In this context, nanofiltration (NF) has emerged as a promising technology due to its ability to selectively remove multivalent ions and low

[a]Department of Chemical Engineering, BITS-Pilani, Pilani, Rajasthan-333031, India. E-mail: somak.chatterjee@pilani.bits-pilani.ac.in; Fax: +91-1596-51-5757; Tel: +91-1596-244183

[b]Department of Chemistry, Anna University, Chennai, Tamil Nadu-600025, India

† Electronic supplementary information (ESI) available. See DOI: https://doi.org/10.1039/d5ra01144b

molecular weight organic molecules, while retaining essential salts, thereby providing high efficiency in treating contaminated groundwater. Polymeric nanofibers are especially attractive in this aspect, having diameters ranging from nanometers to submicron level. They are synthesized from natural and synthetic polymers and can fit into membrane reactors or fixed-bed columns for a wide range of nanofiber-based applications.[14] These fibers provide a diverse foundation of environmental applications, particularly in water treatment to remove heavy metals, persistent organic pollutants (POPs), contaminants of emerging concern (CECs) and oil.[15]

Electrospinning is a prominent nanofiber synthesizing process, alongside interfacial polymerization, phase separation and self-assembly that enables precise control of thickness, porosity, hydrophilicity and polarity.[16] Electrospun nanofibers function well due to their large surface area, fine pores, porous structure, and linked fibers. Optimum electrospinning parameters and precursor compositions (polymers, solvents, and other additives tailored to specific applications) impart these properties. Due to intricate process demands and growing advances, basic nanofibers cannot meet the needs. Coaxial electrospinning provides a feasible option to address the challenges of basic electrospinning by producing core–shell nanofibers with improved efficiency.[15] Composite polymer melts loaded with nanoparticles can be adjusted to selectively remove contaminants, rendering water purification more feasible and effective.[17] Different nanomaterials, such as nanoclays, metal-oxide nanoparticles, carbon nanomaterials and layered double hydroxides (LDHs) can be used.[18] Amongst these, LDHs possess a large surface area, which allows for an increased number of active sites for the adsorption of lead and fluoride ions.[19] Mg–Al LDH has a strong affinity for these ions. This LDH can be uniformly dispersed in polyethersulfone (PES), which is used as a hydrophobic core. On the other hand, polyacrylonitrile (PAN) can be used as a hydrophilic shell for enhanced filtration.[20] Numerous studies show that LDHs have been used alone or in polymers to prepare nanocomposites.[21] However, limited studies have witnessed the synergistic effect of a composite core melt with a pure shell polymer in co-axial electrospun nanofibers.

In the current study, LDH was impregnated in PES (used as a core polymer melt), with PAN as the shell polymer to remove lead and fluoride from a contaminated stream. The prepared co-axial electrospun nanofibers were optimized to achieve the highest lead and fluoride removal efficiency and water permeability by utilizing an optimal ratio of LDH and polymer. Several characterization methods were employed based on surface properties and morphology to describe the structural property of as-synthesized nanofibers. The impact of pH, reusability, temperature, and coexisting ions on the lead and fluoride uptake efficiency of nanofibers was meticulously investigated through equilibrium experiments. Additionally, prepared nanofibers were subjected to vacuum filtration by depositing them on a substrate. The performance of the nanofibers was ultimately assessed using real-time feed extracted from an adjacent impacted source.

2.   Materials and methods

2.1.   Materials

Polyacrylonitrile (PAN, M_w: 150 kDa) polymer and polyethersulphone (PES, M_w: 98 kDa) polymer were procured from e-Spin Nanotech Pvt. Ltd., India. N,N-Dimethylformamide (DMF, density 944 kg m^{-3}); sodium fluoride (NaF, M_w: 42 g mol^{-1}); lead nitrate (Pb(NO$_3$)$_2$, M_w: 331 g mol^{-1}); magnesium nitrate hexahydrate (Mg(NO$_3$)$_2$·6H$_2$O, M_w: 256 g mol^{-1}); aluminum nitrate nonahydrate (Al(NO$_3$)$_2$·9H$_2$O, M_w: 375 g mol^{-1}); dextran standards (M_w: 70 kDa) and polyethylene glycol (PEG, M_w: 10 kDa, 20 kDa, 35 kDa, 100 kDa and 200 kDa) were procured from M/s Merck Pvt. Ltd., India. All the chemical and reagents were used without further purification. The ultra-pure water utilized in this study was processed using the Milli-Q Integral five staged purification system (Merck Millipore).

2.2.   Instruments

The ESI section explains the instruments used in this investigation (Appendix A).†

2.3.   Preparation of LDH

Mg/Al-LDH was synthesized by combining Mg(NO$_3$)$_2$·6H$_2$O and Al(NO$_3$)$_2$·9H$_2$O in a 2 : 1 molar ratio in double distilled water. After a clear solution was obtained, 0.5 g of CTAB was added and stirred until fully dissolved. Gradual addition of 0.5 M NaOH induced the formation of a white solution until pH 10. The solution was stirred for 24 hours until a dense sol was formed. This sol was rinsed with distilled water several times. The resultant gel was subsequently washed and dried at 80 °C for 24 hours. The resulting white powder was calcinated at 400 °C for 12 hours in a muffle furnace. The powder that was obtained (average size: 400 nm) was finely grounded using an agate mortar and pestle and stored in an air-tight container and used for further experimentation.

2.4.   Preparation of electrospun nanofibers

Polymer solutions comprising of PAN and PES were synthesized using DMF as the solvent. Pre-weighed amounts of PAN and PES were dissolved in DMF while stirring to create a clear solution. LDH at 0.1, 0.3, 0.5 and 0.7 wt% was added to PES polymer solution in appropriate ratios and both the PAN–DMF and PES–LDH–DMF solutions were agitated continuously for 24 hours (see Appendix A methodology†). The solutions were heated intermittently to ensure complete dissolution. After simultaneous heating and stirring, the solution was sonicated and brought to room temperature. Both polymer solutions were loaded into a syringe and used in an electrospinning system to prepare core–shell coaxial nanofibers (Fig. 1).[4]

2.5.   Filtration studies

A dead-end ultrafiltration cell was utilized to assess different membrane properties and its permeate flux.[22] Details were presented in the ESI (Appendix B).†
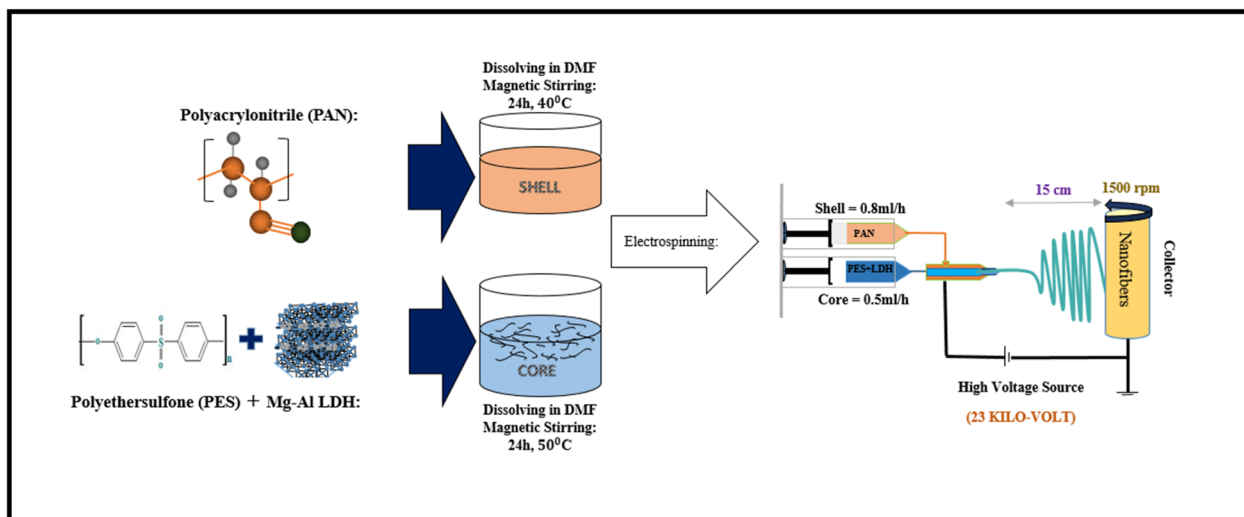
Fig. 1 Schematic of the composite nanofiber preparation.

2.6. Equilibrium studies

The prepared nanofiber's uptake capacity was examined using an equilibrium method at three different temperatures.[4] Details are presented in the ESI (Appendix C).†

3. Result and discussion

3.1. Morphology

Surface morphology, pore size distribution and roughness of the prepared nanofibers were significantly impacted by the inclusion of LDH filler. Fig. 2(i) and (ii) represents SEM micrographs of Mg/Al LDH powder. Micrographs of pure PAN/PES and composite nanofibers with different concentrations (0.1, 0.3, 0.5, and 0.7 wt%) are shown in Fig. 3 and the ESI section (Appendix B).† The average diameter of Mg/Al-LDH powder and nanofibers were analyzed using these micrographs. These micrographs were also analyzed to establish the mechanism of adsorption of Pb^{2+} and F^- in LDH-based nanofibers. The micrographs demonstrated that LDH offers a diverse spectrum of stone-like morphologies, comprising of different sizes and shapes, with particle sizes falling within the range of 3–5 μm, having a surface area of 25 m^2 g^{-1}.[23] However, SEM images reveal that the sample is porous at 100× magnification.

Polymeric PAN/PES nanofibers (N0) have diameters ranging from 200–500 nm (Fig. 3).[24] The average fiber diameter of the nanofibers abruptly increases to 500 nm from 302 nm with a slight degree of irregular and uneven surface morphology upon the addition of 0.1 wt% LDH. However, the average diameter decreased (400 nm) as the LDH concentration was increased to 0.7 wt% (PES/0.3 wt% LDH, PES/0.5 wt% LDH and PES/0.7 wt% LDH). These contrary observations were due to changes in surface tension and electrostatic repulsion in composite solutions.[25] Furthermore, LDH is not only attached or dispersed within the nanofibers (Fig. S1(N3)†), but also detaches from the surface of the nanofibers in the form of flakes when its concentration increases in polymer solution. Free LDH

has high anion exchange capacities and large specific surface areas, and efficiently eliminates and adsorbs contaminants, such as heavy metals, inorganic anions and organic pollutants from wastewater. LDHs encourage the breakdown of hazardous organic waste in water bodies. LDH nanoparticles effectively remove harmful microorganisms from water. Their incorporation with point-of-use technology provides a low-cost and straightforward technique for improving water quality, especially in devastated regions.[60,61] LDH particles begin to agglomerate and form nanometer-scale clusters at higher concentration. According to Othman *et al.*,[26] agglomeration is typically caused by van der Waals attraction forces between nanoparticles. Nano-sized fillers enhance interfiber connections by building LDH particle bridges, creating a conductive network and strengthening ionic conductivity.[27]

The enhanced removal effectiveness of lead and fluoride ions by prepared nanofibers is largely due to the synergistic interaction of LDH particles within the polymer matrix.[28] Incorporating LDH particles into polymer nanofibers creates an ordered structure with an improved specific surface area. For example, pure polymeric nanofibers (N0) have a surface area of 12 m^2 g^{-1} which doubles to 25 m^2 g^{-1} upon the addition of 0.7 wt% LDH. Adsorption–desorption isotherms of N4 nanofibers correlate this finding (Fig. S3†) (Appendix B of the ESI section†). The enhanced surface area provides more active sites for pollutant adsorption, which improves total removal efficacy. LDHs have positively charged layers and exchangeable interlayer anions, allowing them to attract and interchange negatively charged fluoride ions in water. When incorporated within the polymer matrix, these LDH particles ensure their ion-exchange properties and effectively remove fluoride ions from aqueous solutions. Functional groups in the polymer matrix and LDH particles can interact with lead ions *via* chelation or complexation pathways. This in turn increases the binding affinity, making it easier to remove them from water. However, an appropriate LDH concentration must be selected to balance mechanical stability and filtration efficacy. Thereby, an
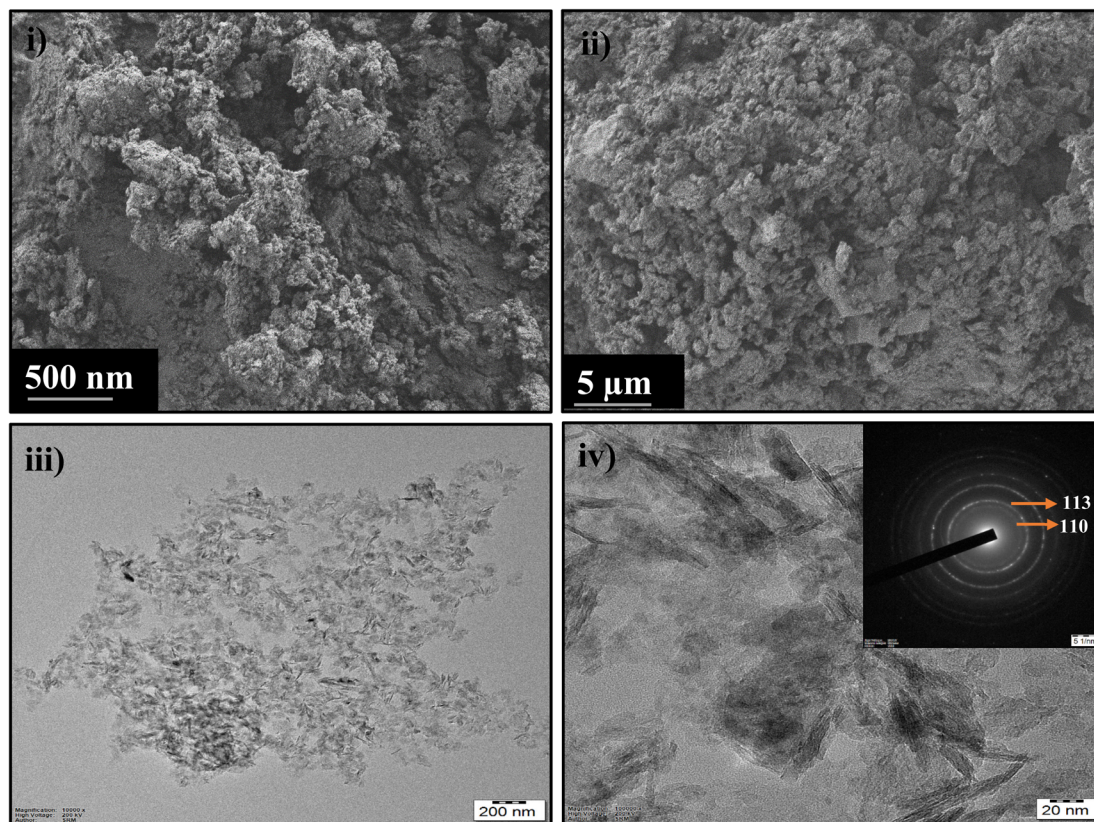
Fig. 2 (i and ii) SEM images showing the morphology of LDH. (iii and iv) TEM micrographs revealing the internal structure; the inset displays the corresponding SAED pattern.

optimum amount of LDH was selected as per the information presented in Table 1. Different parameters such as porosity and permeability were presented. For example, the porosity of the N0 nanofibers is 26%, which increases to 49% for N4 nanofibers. Similarly, membrane permeability increases from 1×10^{-12} m Pa^{-1} s^{-1} (N0 nanofibers) to 5×10^{-12} m Pa^{-1} s^{-1} (N4 nanofibers). Nanofibers with higher porosity exhibit enhanced water flow rates, but they demonstrated a minor reduction in their ability to remove lead and fluoride.[29] An appropriate balance between water throughput and pollutant removal was achieved by identifying a certain range of porosity. A similar trend was seen in the case of hydrophilicity (contact angle). For example, the contact angle of N0 nanofibers (measured by the sessile drop method) is 64°. However, N1, N2, N3 and N4

nanofibers have greater contact angles of 93°, 92°, 99° and 91°, respectively, representing their hydrophobic nature, resulting in reduced fouling rates and filtration performance. The addition of Mg–Al LDH to the PAN–PES solution resulted in a decrease in viscosity, which impacted electrospinning process. The viscosity of the polymeric solution is a significant factor in this context.[22] For instance, the viscosity of pure polymeric solution (utilized to synthesize N0 nanofibers) is 110 mPa s. However, the viscosity reduces to 12 mPa s when the percentage of LDH in the PES polymer is increased to 0.7 wt%. As a result, bead production and the diameter of the nanofibers are reduced when the viscosity of the core polymer solution decreases (Table 1). N4 nanofibers with noticeably higher lead and fluoride removal efficiency (66% for lead and 70% for
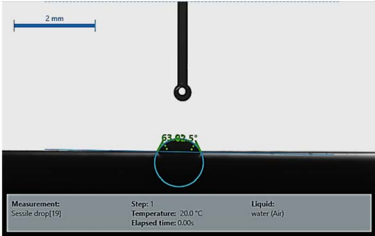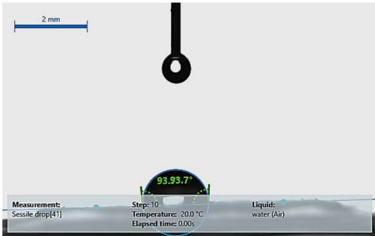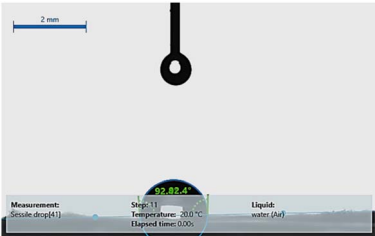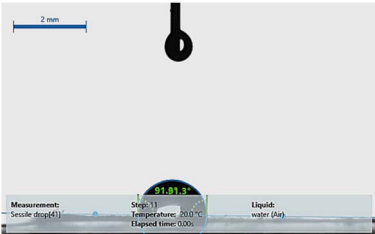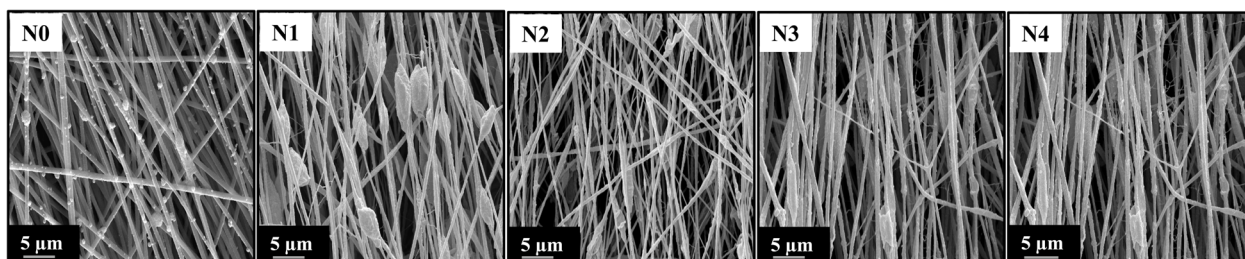

Fig. 3 SEM micrographs of the composite nanofibers.

Table 1 Nomenclature of different electrospun nanofibers[a]

Nomenclature	LDH (gm)	Permeability (m s⁻¹ Pa⁻¹) × 10¹²	Porosity (%)	Contact angle (°)	Droplet over nanofibers (photographic visualization)	Viscosity of core polymer (mPa s)	Surface area (m² g⁻¹)	Fluoride rejection (%)	Lead rejection (%)
N0	0	1	26	64		110	12	46	39
N1	0.01	2	40	93		8	17	40	65
N2	0.03	2	41	92		19	18	66	53
N3	0.05	3	42	99		9	15	10	65
N4	0.07	5	49	91		12	25	70	66

[a] All samples were prepared using 6 wt% PAN and 10 wt% PES, and the viscosity of shell side polymer was 940 mPa s. All measurements are subjected to 5% error.

fluoride) were produced by combining the ideal configurations obtained by the LDH ratio, porosity, contact angle and viscosity. N4 nanofibers that incorporated Mg–Al LDH into the PAN–PES matrix offered improved structure for lead and fluoride removal. Elemental composition of LDH and LDH-based nanofibers was investigated using energy-dispersive X-ray spectroscopy (EDX). Micrographs of LDH and nanofibers are displayed in Fig. 4. The essential components in the composition of LDH and nanofibers are carbon (C), oxygen (O), sulfur (S), magnesium (Mg) and aluminum (Al). For example, 74 wt% of N4 nanofibers is carbon, 23 wt% is oxygen, 1.04 wt% is sodium, 1.02 wt% is aluminium and 0.26 wt% of magnesium.
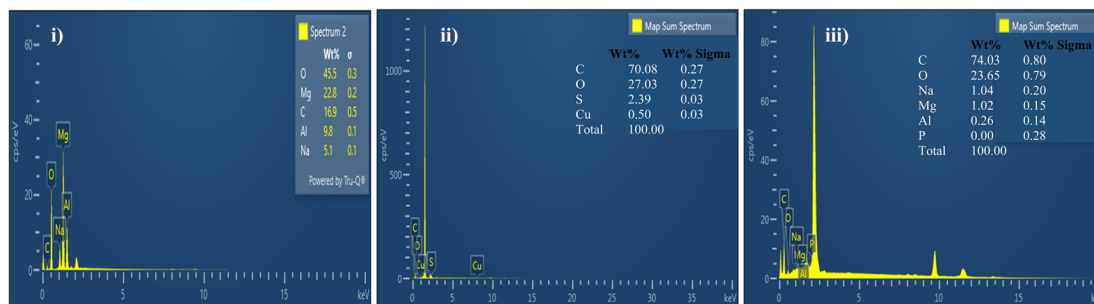
Fig. 4 EDS spectrum of the (i) LDH powder (ii) N0 and (iii) N4 nanofibers.

EDX mapping was employed to study the elemental distribution of Mg and Al within the nanofiber matrix, showing successful incorporation and dispersion of LDH. Detailed micrographs are shown in the ESI section (Fig. S2).† Effective integration of LDH into the polymer network is observed, with magnesium (Mg) and aluminum (Al) signals evenly distributed throughout the nanofiber structure. A homogenous distribution indicates strong polymer–LDH interactions, resulting in better functioning in applications such as water filtration. However, isolated high-intensity zones in the EDX map may suggest LDH agglomeration, which might affect composite performance. Therefore, the elemental mapping offers vital information on the structural homogeneity and dispersion effectiveness of LDH inside the nanofibers.

3.2. Transmission electron microscopy (TEM) analysis

Transmission electron microscopy (TEM) investigations were conducted to gain a comprehensive understanding of the thermal calcination process of LDHs, as well as different crystallographic transitions that occur prior to calcination. Fig. 2(iii) and (iv) displays the TEM images of LDH along with the SAED micrographs. The material was synthesized to possess a precisely defined hexagonal shape with a crystallographic structure. The interplanar distance is $d = 0.312$ nm (as determined from the figure). The SAED patterns exhibit Debye–Scherrer rings that correlate with the diffraction from the distinctive atomic planes (1 1 3) and (1 1 0) of LDH nanoparticles, as shown in the inset of Fig. 2(iv). EDX data indicates the presence of 22.8% magnesium (Mg) ions and 9.8% aluminum (Al) ions in the composition of the LDH (Fig. 4).

3.3. Mineralogical phases

Mineral phases of PAN–PES composite nanofibers are shown in Fig. 5. Crystal planes exhibited a strong and distinct reflection, indicating the presence of a layered phase with an interlayer molecular structure, verifying the crystalline nature of the LDH.[30] The peak of Mg/Al LDH $2\theta = 23.26°$ correlates with the (006) planes of the hydrotalcite structure. Broad peaks at 39.50° (015) and 47.12° (018) suggest the occurrence of a hexagonal LDH lattice.[31] The presence of diffraction peaks at 63.06° (110) and 65.20° (113) indicate that magnesium and aluminium are evenly distributed within the nanofibers.[32] The amorphous nature of both PAN–PES polymers is shown by characteristics

peak observed at $2\theta = 18°$. In addition, the peak at an angle of $2\theta = 45.5°$ reflects the carbon pair in the subsequent chain. Furthermore, diffraction peaks of composite nanofibers were indicative of the polymer (PAN) semi-crystalline characteristics and presence of unique sulfone groups of PES, suggesting the existence of both polymers in the composite. There were no substantial changes in the highest points of the data, indicating that the addition of Mg–Al LDH to the PAN–PES nanofibers did not alter the original polymer structures.[33] Diffraction peaks at 63.06° ((110) plane) and 65.20° ((113) plane) in X-ray diffraction (XRD) patterns often correspond to the crystalline structure of Mg–Al LDHs. These peaks represent the periodic arrangement of magnesium and aluminum in the LDH lattice. However, the presence of the (113) peak at 65.20° in the N0 sample, which excludes LDH, demonstrates that this peak is not limited to LDH structures. This anomaly might be attributed to the intrinsic crystallinity of the PES polymer matrix employed in the nanofibers. XRD spectra of pure PES membranes also exhibit peaks at this angle, showing that (113) reflection is unique to the PES structure.[62] Therefore, the diffraction peak at 65.20° in the N0 sample likely arises from the crystalline domains of the polymer matrix rather than the presence of LDH.
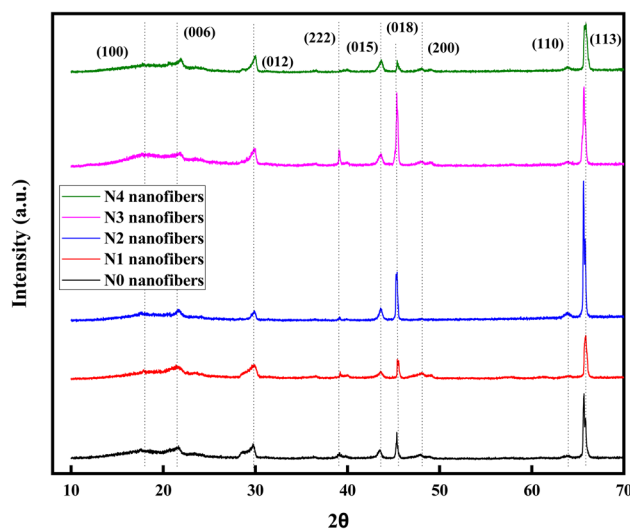

Fig. 5 XRD analysis of N0, N1, N2, N3, and N4 nanofibers.

3.4. Functional groups

Functional groups determined by FTIR spectra of the PAN and PES polymer with the prepared nanofibers were shown in Fig. 6. These spectra demonstrate absorption bands at specific wavenumbers, which indicate the presence of different functional groups in the composite nanofibers. The absorption band at 2240 cm^{-1} is due to nitrile (C≡N) stretching vibrations, which is characteristic of the PAN polymer. Moreover, stretching vibrations of aromatic ring structures (C=C) are responsible for the peaks in the 1450–1600 cm^{-1} range, suggesting PAN polymer crystallinity. Both polymer powders and nanofibers have absorption peaks around 2900–3100 cm^{-1} that correlate with the tensile vibration peak of the (–CH–) aliphatic group. Furthermore, significant absorption bands between 1100–1240 cm^{-1} correspond to symmetric and asymmetric stretching of sulfone (SO$_2$) group. In addition, the absorption bands at 1250 cm^{-1} and 1160 cm^{-1} indicate the presence of ether linkages (C–O–C) in the PES structure. Significantly, wide absorption band at 3400–3600 cm^{-1} are affiliated with the (O–H) stretching vibrations, which are indicative of hydroxyl groups found in the hydrotalcite structure of Mg–Al LDH. The presence of hydroxyl groups demonstrates successful integration of Mg–Al LDH within nanofibers, which contributes to composite material's potential hydrophilicity. Furthermore, absorption bands at 1640 cm^{-1} are connected with the stretching vibrations of (C=O) groups, indicating the presence of PAN in the composite.[34] PES incorporation into the nanofibers was confirmed by identifying the distinctive sulfone (S=O) stretching vibrations at 1150 cm^{-1} and 1030 cm^{-1}. Other peaks at 563 cm^{-1} and 750 cm^{-1} suggest that LDH was successfully impregnated into PES (core polymer). This is due to the tensile vibration peak of M–O and bending vibration peak of M–OH (M=Mg and Al in the octahedral main layer) between 400–800 cm^{-1}. Lead and fluoride adsorption onto N4 nanofibers causes binding interactions that alter the peak of O–H and C=O groups. New peaks arise between 400 cm^{-1} and 900 cm^{-1}, indicating metal–oxygen and metal–fluoride connections. Adsorption also involves chelation and ion exchange responses as evidenced by the widening of functional group peaks.

3.5. Thermal analysis

Thermogravimetric analysis (TGA) is a thermal analysis technique in which changes in the physical and chemical characteristics of materials are assessed as a function of rising temperature (with a constant heating rate) or time (with a constant temperature and/or mass loss). Processes such as vaporization, sublimation, absorption, adsorption, desorption, chemisorption, breakdown and oxidation/reduction were determined using TGA. The thermal stability of the prepared nanofibers is presented in Fig. 7. TGA analysis suggests that the inclusion of LDH drastically improves the thermal stability of nanofibers compared with pristine polymer nanofibers. LDH nanofiller displays a multi-step breakdown process, with initial weight loss due to the elimination of interlayer water (~100–200 °C) and enormous degradation that occurs between 300–500 °C due to dehydroxylation and anion decomposition, leaving behind thermally stable metal oxides.[35,36] On the other hand, pure nanofibers (N0) degrade quickly in a single step at temperatures between 300 and 500 °C, suggesting little residual mass and poor heat resistance. However, LDH-containing nanofibers (N4) exhibit a more gradual weight loss profile, higher residual mass, and delayed decomposition (~350–550 °C), indicating that LDH functions as a thermal barrier by limiting the mobility of polymer chains and creating a protective layer.[37] LDH-incorporated nanofibers exhibit better heat resistance. The improved thermal resistance of LDH-incorporated nanofibers makes them more suitable for high-temperature applications, such as filtration and membrane technologies.

3.6. Photoluminescence spectra

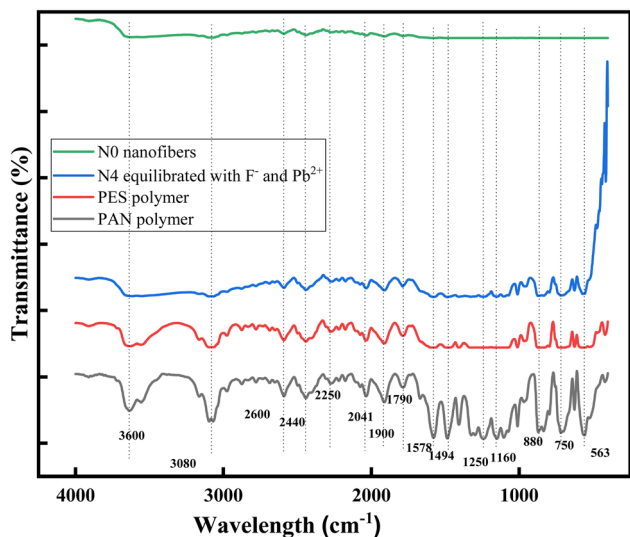Photoluminescence spectra (determined by X-ray photoelectron spectroscopy, XPS) was employed to examine the chemical

Fig. 6 FTIR analysis of PAN powder, PES powder, and the N0 and N4 nanofibers.
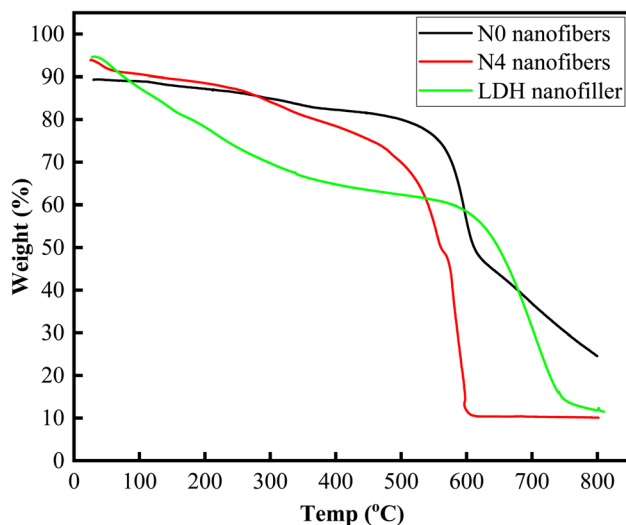

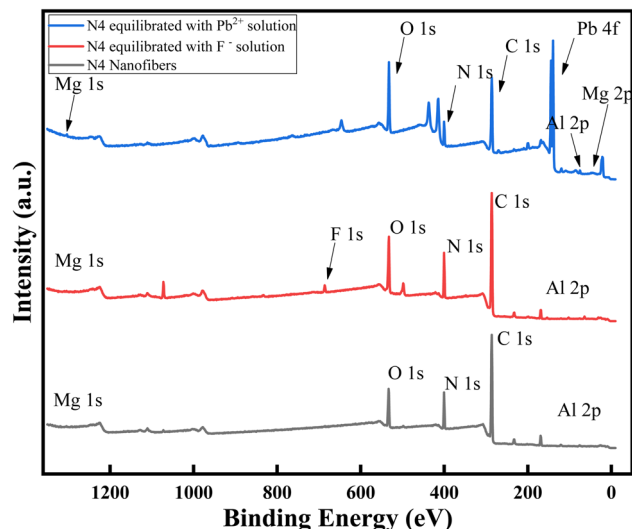**Fig. 7** TGA analysis of LDH powder and the N0 and N4 nanofibers.

Fig. 8 XPS analysis of the N4 nanofibers.

states and compositions of elements on adsorbents, indicating significant information about lead and fluoride adsorption onto nanofibers. XPS spectra of Mg–Al LDH impregnated on PAN–PES nanofibers before and after analyte (lead and fluoride) adsorption was depicted in Fig. 8. The wide-scan XPS spectra peak positions of aluminum, oxygen and carbon (Fig. 8) are comparable with those in our prior study.[38] In this spectra, peaks of magnesium, fluorine and lead are also visible. The Mg(2p) signal was detected at a binding energy of approximately 50.1 eV, while Al(2p) peak was observed at 75.1 eV.[9] The existence of carbon-based chemicals in nanofibers is indicated by a peak at 284.6 eV corresponding to C(1s). Peaks are typically linked to carbon–carbon (C–C) and carbon–hydrogen (C–H) bonds. The O(1s) peak was detected at a binding energy of 531 eV, indicating the presence of carbonyl (C=O) and hydroxyl groups (OH), as well as water molecules within the LDH layers and on the surface.[4] The presence of OH groups is crucial in adsorption mechanisms, especially in the case of lead ions, where it occurs through surface complexation.[39] In the case of fluoride ions, adsorption occurs through ion exchange and hydrogen bonding.[40] Anticipated changes in the binding energies of these peaks and the emergence of additional peaks corresponding to Pb(4f) and F(1s) were expected upon interaction with lead and fluoride solutions. The detection of Pb(4f) peaks would suggest that lead ions have been effectively adsorbed onto the surface of the composite, probably through interactions with the hydroxyl groups and oxide surfaces of Mg and Al. Similarly, the identification of F(1s) peaks would provide evidence of fluoride ion adsorption, potentially aided by ion exchange with hydroxyl ions in the LDH structure and electrostatic attractions.

3.7. Equilibrium study

An equilibrium study was performed to determine N4 nanofiber's uptake capacity at different pH, temperatures and coexisting ions. Experiments were performed using synthetic lead

and fluoride solution (between 1–2200 mg L^{-1}) agitated in an orbital shaker.

3.7.1. Effect of temperature. The impact of temperature on the uptake performance of N4 nanofibers for removing ions from aqueous solutions was investigated. Understanding the effects of temperature is critical for optimizing the operational parameters of water treatment systems using composite nanofibers. This study was conducted with an initial concentration ranging from 10–2200 mg L^{-1} for lead and fluoride at 298 K, 308 K and 318 K (Fig. 9a and b). The uptake of lead ions by the nanofibers increases with temperature. For example, the uptake capacity of lead by N4 nanofibers is 99 mg g^{-1} at 298 K, which increases to 200 mg g^{-1} at 308 K and 300 mg g^{-1} at 318 K at an equilibrium concentration of 1200 mg L^{-1} (Fig. 9a). The uptake capacity for lead removal increases at higher temperatures, suggesting that the adsorption process is endothermic. Lead ions are considered to be mobile and interact more with the adsorption sites on the Mg–Al LDH as a result of the temperature increase. This can be attributed to the endothermic nature of the interactions between the free lead ions and the hydroxyl ions of the nanofibers.[41] Also, the uptake capacity of N4 nanofibers increases with equilibrium concentration. For example, the uptake capacity is 70 mg g^{-1} at an equilibrium concentration of 690 mg L^{-1}, which increases to 100 mg g^{-1} at an equilibrium concentration of 1200 mg L^{-1}. At a higher equilibrium concentration, increased levels of solute (lead) are present in the feed, which are captured by the empty active sites.[42] In this study, lead uptake stabilizes and slightly increases when the concentration increases over 800 mg L^{-1}. For example, uptake capacity remains at 100 mg g^{-1} between 800 mg L^{-1} and 1200 mg L^{-1}.

Similar to the previous trend, fluoride uptake by N4 nanofibers increases with temperature. For example, fluoride uptake capacity by N4 nanofibers is 100 mg g^{-1} at 298 K, which improves to 201 mg g^{-1} at 308 K and 363 mg g^{-1} at 318 K at an equilibrium concentration of 2000 mg L^{-1} (Table 2). At higher temperature, kinetic energy of fluoride ions increases, leading to enhanced ion mobility and a higher frequency of collisions between fluoride ions and the surface of LDH. This increased molecular motion accelerates the diffusion of fluoride ions towards active adsorption sites on LDH surface. This phenomenon improves the adsorption kinetics. Moreover, higher temperatures can induce slight thermal expansion or increased flexibility of the interlayer spaces within the LDH structure. This enhanced interlayer mobility facilitates more efficient ion exchange between fluoride ions and intercalated anions (*e.g.*, carbonate or hydroxide) within LDH layers. As a result, elevated temperature promotes greater accessibility to adsorption sites and enhances the overall ion-exchange capacity of the material.[43] Therefore, elevated temperatures enhance molecular mobility and improved diffusion rates, which in turn improve the nanofibers' ability to uptake fluoride.[44] Also, the uptake capacity of N4 nanofibers increases with equilibrium concentration. For example, the uptake capacity is 160 mg g^{-1} at an equilibrium concentration of 640 mg L^{-1}, which increases to 363 mg g^{-1} at an equilibrium concentration of 1500 mg L^{-1}. At an increased equilibrium concentration, higher levels of solute
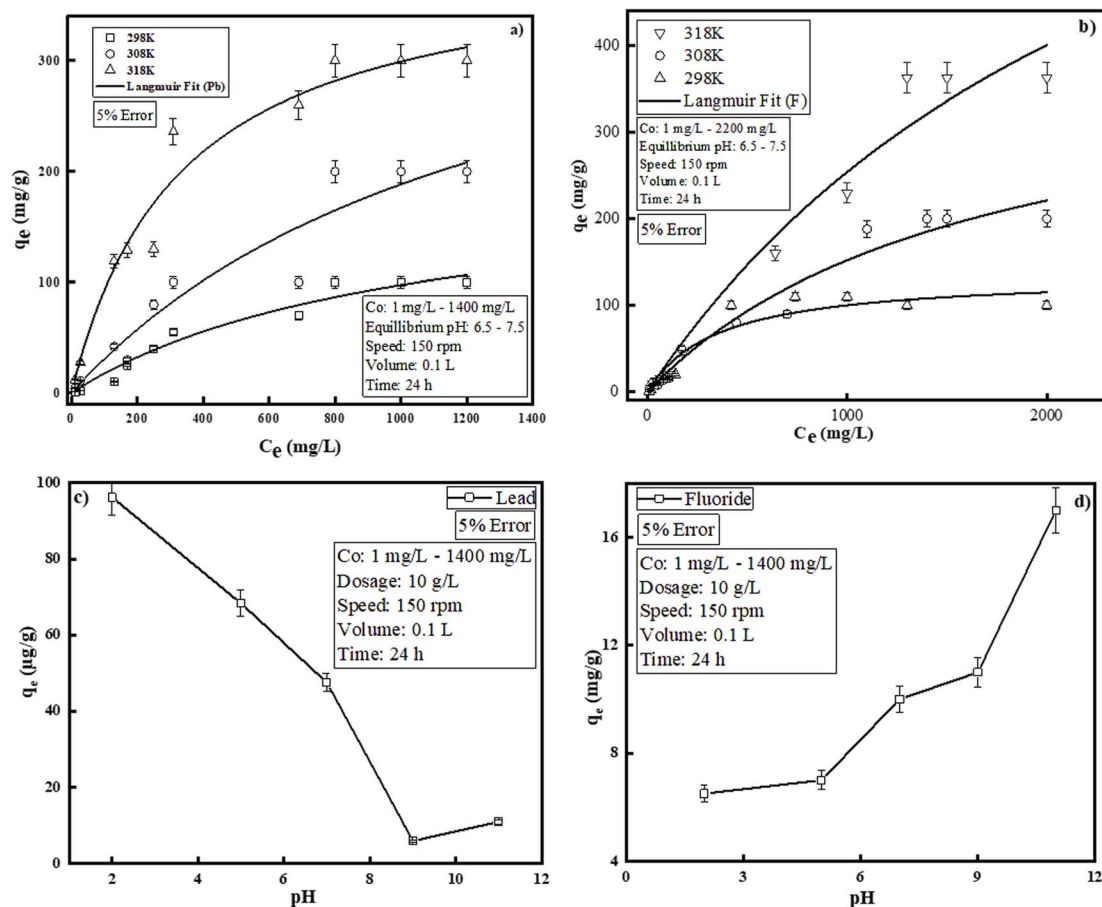
Fig. 9 Adsorption isotherm studies of (a) lead and (b) fluoride. Effect of the pH values on the uptake capacities of (c) lead and (d) fluoride using the N4 nanofibers.

Table 2 Langmuir adsorption isotherm parameter

Temperature (K)	Type	Langmuir isotherm			Freundlich isotherm		
		V_m (mg g^{-1})	K (L mg^{-1})	ARE (%)	n (dimensionless)	K_f (mg^{1-n}(L g^{-1})^n)	ARE (%)
298	Fluoride	948	0.00036	8.9	3.32	1.982	8
	Lead	196	0.00098	10	1.43	0.805	35
308	Fluoride	884	0.00025	8.6	1.14	0.369	12
	Lead	438	0.00075	35	1.29	1.386	40
318	Fluoride	135	0.00284	11	0.74	0.022	29
	Lead	398	0.00303	89	2.12	11.72	81

(fluoride) are present in the feed, which are captured by the empty active sites.[4] This study shows that fluoride uptake stabilizes and slightly increases when the concentration rises over 1300 mg L^{-1}. For example, the uptake capacity is maintained at 360 mg g^{-1} between 1300 mg L^{-1} and 2000 mg L^{-1}.

3.7.2. Effect of pH. The uptake capacity of N4 nanofibers exhibits a significant dependence on the pH of the solution, directly influencing their removal efficiency for lead and fluoride ions. Understanding the impact of pH on the adsorption mechanism provides valuable insight into functional performance of these nanofibers. In terms of lead removal, an acidic

environment clearly promotes higher lead uptake (Fig. 9c). For example, 96% of lead ions were removed at pH 2, while removal efficiency decreases to 68% at pH 5, 46% at pH 7, 6% at pH 9 and 11% at pH 11. Enhanced uptake in acidic conditions can be attributed to several factors. For example, increased availability of free lead ions, improved ion-exchange capability of LDH layers and electrostatic attraction between positively charged lead ions and the negatively charged LDH surface. However, in alkaline conditions, lead ions precipitate as hydroxide salt, reducing the concentration of free lead available for adsorption. Additionally, the surface charge of LDHs becomes less

conducive for lead interaction and competition with hydroxide ions further decreases lead uptake.[45]

In contrast, the fluoride removal profile demonstrates an opposite trend across the same pH range (2–11) (Fig. 9d). Maximum fluoride removal of 20.73% occurred in alkaline conditions at pH 11, while the removal efficiency decreased to 11.7% at pH 9, 10.4% at pH 7, 7% at pH 5 and negligible removal was observed at pH 2. Superior fluoride uptake in alkaline environment is attributed to the stability of fluoride ions in these conditions and reduced competition for adsorption sites. In alkaline solutions, the LDH surface retains a positive charge, facilitating electrostatic attraction and ion exchange between LDH layers and fluoride ions. Conversely, higher concentration of hydrogen ions compete with fluoride ions for adsorption sites on LDH in an acidic environment, significantly inhibiting fluoride uptake. This competition, combined with the relatively low affinity of LDH for fluoride under acidic conditions accounts for reduced removal efficiency.[46]

3.7.3. Effect of coexisting ions on the uptake performance.

The effect of co-existing ions on N4 nanofiber's uptake capacity was examined using solutions containing fluoride (5 ppm) and lead (1 ppm), while varying the concentration of the coexisting ion. Rejection percentages indicate a notable reduction in nanofiber uptake capacity in the presence of fluoride and lead, compared with solutions containing only single ion (Table 3). At a concentration of 1 mg L^{-1}, the lead removal efficiency of N4 nanofibers is 66%. At this same lead concentration, the removal efficiency of N4 nanofibers decreases to 52% when the fluoride concentration is kept at 50 μg L^{-1}. Furthermore, the N4 nanofiber removal capacity drops to 45% when the fluoride concentration rises to 100 μg L^{-1} (the lead concentration is kept constant at 1 mg L^{-1}). A similar observation was observed in the case of fluoride removal by N4 nanofibers. When no coexisting ions are present, the fluoride removal efficiency of N4 nanofibers is 70% at 5 mg L^{-1}. However, fluoride removal efficiency decreases to 3% at a lead concentration of 50 μg L^{-1}. However, the removal efficiency marginally increases to 12% when the lead concentration increases to 100 μg L^{-1}. These results

suggest that the presence of lead and fluoride ions significantly hinders their respective adsorption, as they compete for available active sites. The positively charged lead strongly interacts with the hydroxyl groups on the LDH surface, facilitating its adsorption. However, the fluoride anion does not entirely inhibit lead uptake, although its presence reduces the overall rejection efficiency.[47]

3.7.4. Dynamic filtration.

The dynamic filtration study of N4 nanofibers is shown in Fig. 10. Detailed methodology was described in the ESI section (Appendix B).† For each experiment, separate nanofibers were used for 15 hours of filtration. A filtration period of 15 hours was chosen based on the observed breakthrough time, at which the permeate concentration exceeds WHO standards (see Section 1). In the case of lead removal (Fig. 10a), the lead concentration sharply increases with longer vacuum filtration time. For example, for an initial feed concentration of 100 μg L^{-1}, the lead concentration is 6 μg L^{-1} after two hours of filtration, which increases to 39 μg L^{-1} after 12 hours of filtration. When the feed concentration increases to 150 μg L^{-1}, the lead concentration in the permeate increases to 5.9 μg L^{-1} and 68 μg L^{-1} after two hours and 12 hours filtration, respectively. At a feed concentration of 200 μg L^{-1}, the lead concentration in the permeate increases to 3.5 μg L^{-1} and 70 μg L^{-1} at two hours and 12 hours of filtration, respectively. This happens because of weak binding interactions between LDH and lead ions, resulting in desorption. Furthermore, the active sites in the nanofibers become saturated, reducing the retention of ions, resulting in increased permeate concentration. Synthetic lead solution was used for this experiment. However, the lead concentration in the permeate remains below 10 μg L^{-1} (WHO limit lead concentration of 15 μg L^{-1} for 12.45 hours of real life feed solution). The breakthrough time is 4.45 hours, 5.42 hours and 6.25 hours for initial feed concentrations of 100 μg L^{-1}, 150 μg L^{-1} and 200 μg L^{-1}, respectively using a synthetic solution. Lead is present in extremely small concentrations in real life feed, which enhances the breakthrough time, despite the several other impurities. A similar trend was noted during the filtration of fluoride ions (Fig. 10b). For example, for an initial feed concentration of 5 mg L^{-1}, the fluoride concentration is 2.5 mg L^{-1} after two hours of filtration, which increases to 5.6 mg L^{-1} after 12 hours of filtration. When the feed concentration increases to 10 mg L^{-1}, the concentration of fluoride in the permeate increases to 6 μg L^{-1} and 7.3 μg L^{-1} at two hours and 12 hours filtration time, respectively. At a feed concentration of 20 mg L^{-1}, the lead concentration in the permeate increases to 11 mg L^{-1} and 16 mg L^{-1} at two hours and 12 hours filtration time, respectively. This happens because active sites in the nanofibers become saturated, which reduces the retention of ions. Fluoride ions are tiny and monovalent, making selective adsorption more difficult. Removal of fluoride frequently uses specialized materials like bone char or activated alumina because of their greater affinity for fluoride ions. If non-specialized or exhausted media are employed, filtration efficacy declines with time, resulting in higher fluoride levels in the filtrate. Although a synthetic fluoride solution was used for these experiments, the fluoride concentration in the permeate

Table 3 Effect of coexisting ions on the lead and fluoride uptake by nanofibers[a]

Type	Concentration (lead in feed: 1 mg L^{-1})	Rejection (%)
Pb only	No co-ions	66
F	50 μg L^{-1}	52
	100 μg L^{-1}	45

Type	Concentration (fluoride in feed: 5 mg L^{-1})	Rejection (%)
F only	No co-ions	70
Pb	50 μg L^{-1}	3
	100 μg L^{-1}	12

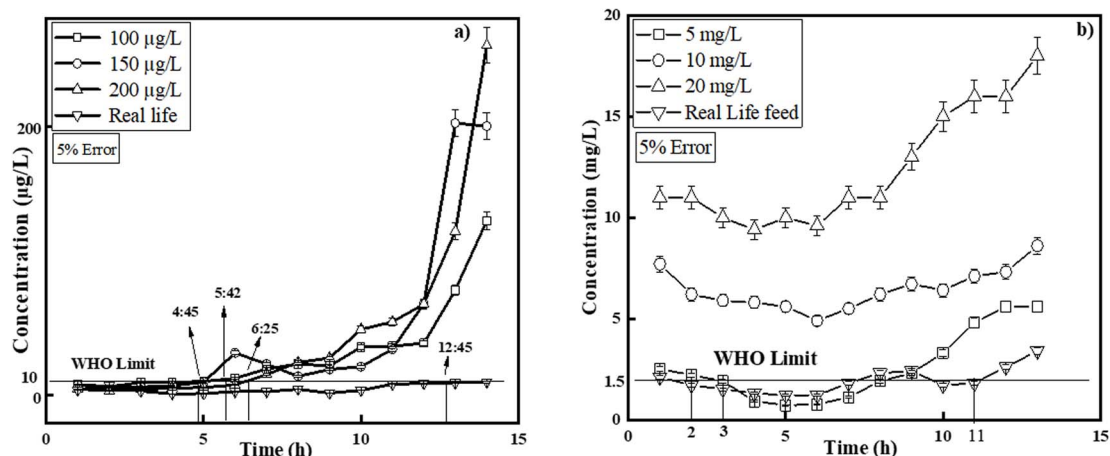[a] All measurements mentioned in the table are subjected to 5% error.

Fig. 10 Dynamic filtration studies for (a) lead and (b) fluoride ions using the N4 nanofiber during vacuum funnel filtration.

remains below 3 mg L^{-1} (WHO limit) after 11 hours in real world feed solution (fluoride concentration: 3 mg L^{-1}). However, the breakthrough time is 11 hours for an initial feed concentration of 5 mg L^{-1} for the synthetic solution.[4]

The average flux of lead permeation is 6.3 L m^{-2} h^{-1}, 17.4 L m^{-2} h^{-1} and 11.8 L m^{-2} h^{-1} at 100 μg L^{-1}, 150 μg L^{-1} and 200 μg L^{-1}, respectively. The average flux of fluoride permeation is 7.47 L m^{-2} h^{-1}, 8.96 L m^{-2} h^{-1} and 9.26 L m^{-2} h^{-1} for at 5 mg L^{-1}, 10 mg L^{-1} and 20 mg L^{-1}, respectively. The average flux for real life feed is 12 L m^{-2} h^{-1} and 3.3 L m^{-2} h^{-1} for lead and fluoride, respectively.[48] There is a contradictory phenomenon arising from the vacuum filtration studies. Conventionally, permeate flux should be lower than pure water flux.[49] The average pure water flux should be 1.8 L m^{-2} h^{-1} at 0.1 mPa (permeability of N4 nanofibers is 5×10^{-12} m s^{-1} Pa^{-1}) as calculated from previous literature.[50] However, the permeate flux mentioned above is higher that pure water flux. Higher permeate flux may arise from concentration polarization, slip flow effects and non-linear flow behavior, typical of post-Darcian regimes. These variations demonstrate how well nanofibers function in filtration applications, particularly in situations involving high flux and concentrated solution.[51]

3.7.5. Regeneration studies. Nanofibers with the highest lead and fluoride uptake capacity were selected for regeneration experiments. The reusability of nanofibers containing fluoride and lead ions was examined after 24 hours of equilibration. Subsequently, nanofibers were regenerated by desorption with 0.01 M of NaOH for fluoride regeneration and 0.01 M of HCl for lead regeneration studies, for 24 hours. First, the nanofibers were equilibrated with an artificial solution containing a predetermined concentration of lead and fluoride ions in an orbital shaker. After 24 hours, the nanofibers were desorbed using 0.1 M of HCl and NaOH solutions followed by washing at a neutral pH (7.0 ± 0.5). The concentration of lead and fluoride solution was determined before and after equilibration with nanofibers. Comparison of uptake capacities throughout regeneration cycles is shown in Fig. 11. This graph shows that adsorption decreases with each subsequent cycle. For example,

the initially fluoride uptake capacity was 363 mg g^{-1}, which decreases to 199 mg g^{-1}, 129 mg g^{-1}, 49 mg g^{-1}, 19 mg g^{-1} and 14 mg g^{-1} in the second-, third-, fourth-, fifth-, and sixth cycle, respectively. A similar trend is observed for lead ion uptake. For example, the initially lead ion uptake capacity was 299 mg g^{-1}, which decreases to 134 mg g^{-1}, 67 mg g^{-1}, 22 mg g^{-1}, 13 mg g^{-1} and 9 mg g^{-1} at the second-, third-, fourth-, fifth- and sixth cycle, respectively. The decrement is attributed to the loss of functionally active sites that were previously present during the uptake of lead and fluoride.[52]

3.7.6. Uptake mechanism. The uptake of lead and fluoride onto N4 nanofibers is addressed graphically in Fig. 12. Lead uptake occurs *via* adsorption onto LDH, primarily through the exchange of ions from cations present in LDH, such as, H$^+$, Mg^{2+} and Al^{3+}.[53] Also, the uptake of lead ions onto the LDH surface can be attributed to the formation of lead hydroxides from lead ions leading to their precipitation in solution. This precipitated hydroxide is probably deposited onto the surface of LDH impregnated nanofibers.[54] The deprotonation of hydroxyl
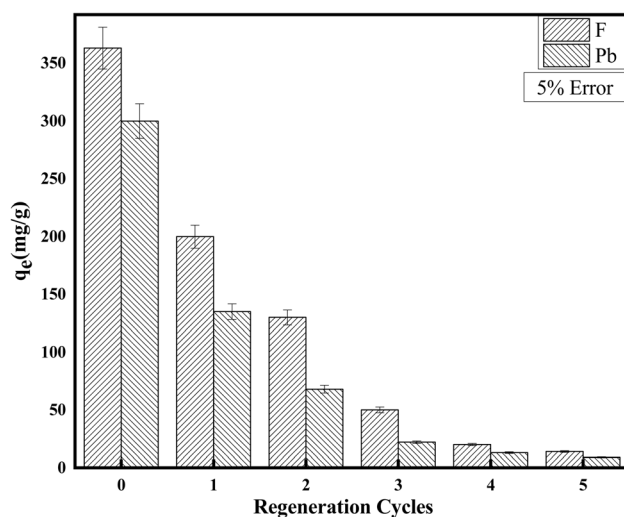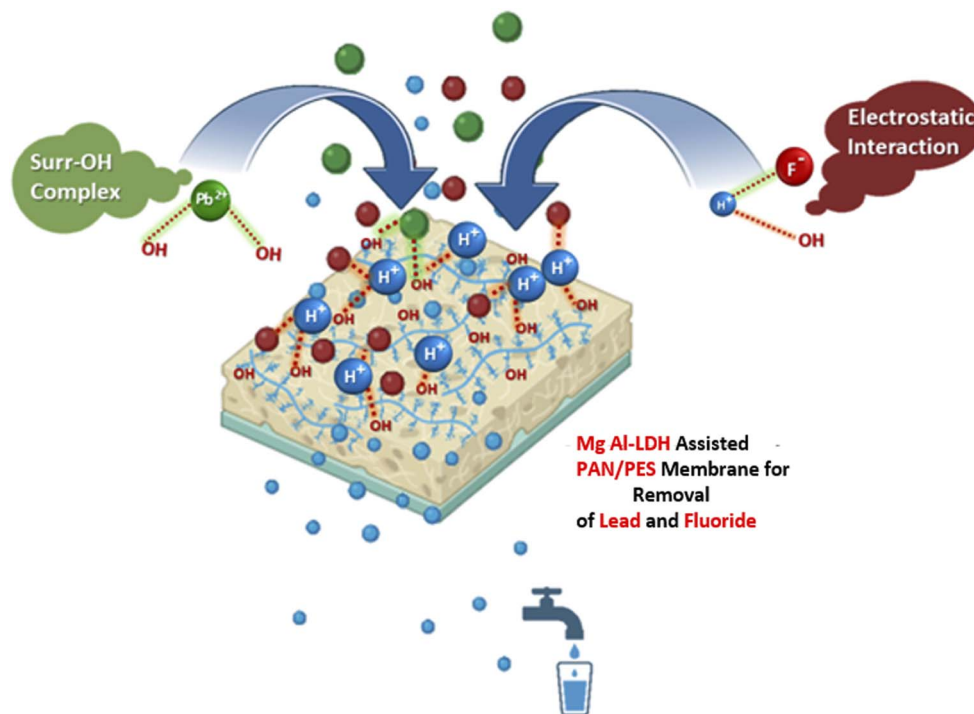

Fig. 11 Regeneration studies.

Fig. 12 Uptake mechanism of lead and fluoride.

groups, which produces surface-bound OH$^-$ complexes, further increases lead uptake. The interlayer anions of LDH also move out and form lead based complexes. Moieties such as carboxylic groups react strongly with lead ions compared to hydroxyl groups.[55] Similar to this, the fluoride removal mechanism is influenced by many factors, such as pH of the solution, the resident time, LDH concentration and interference with other ions present in water.

The uptake mechanism of fluoride ions primarily occurs due to electrostatic interactions between LDH and fluoride ions, followed by ion exchange. Initially, hydroxide ion is protonated. The positive charge of the ion attracts the negatively charged anion from the fluid, adsorbing it onto its surface. Fluorine has a higher electronegativity and bonds with metal on the surface, while water is released in its place.

$$-MOH(s) + H_2O \rightarrow -MOH_2^+(s)$$

$$-MOH_2^+(s) + F^- \rightarrow -MF + H_2O$$
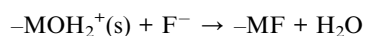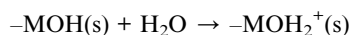
Here, protonation occurs at the hydroxide ion, forming a positively charged ion that will interact more strongly with the fluoride anion. The electrostatic interactions and ion exchange will allow greater fluoride adsorption on the activated sites.

3.7.7. Cost analysis and comparison. The core–shell composite nanofibers developed in the current study have greater uptake capacity and cost-effectiveness for the removal of lead and fluoride, evidenced by an empirical analysis (Table 4). Reverse osmosis membranes (\$300 per m^2) optimally eliminate fluoride (>95%) but struggle to remove lead.[56] However, carbon-based nanofibers (\$300 per m^2) have lead uptake capacity ranging from 50–300 mg g^{-1} and fluoride from 10–50 mg g^{-1}.[57] Metal oxide-embedded fibers (\$250 per m^2) achieve 250 mg g^{-1} of lead uptake and 60 mg g^{-1} for fluoride.[58] Cellulose-based nanofibers (\$150 per m^2) have an uptake of 30 mg g^{-1} for both contaminants.[59] Pure PAN/PES nanofibers (\$84 per m^2) achieve a fluoride uptake of 110 mg g^{-1} but a lower lead uptake of 38 mg g^{-1}.[4] The PAN–PES/LDH nanofibers developed in this study significantly outperform alternatives, achieving lead uptake of 300 mg g^{-1} and 363 mg g^{-1} for fluoride (Table S1†). The cost of LDH and N4 nanofibers also show similar outperformance characteristics (Tables S2 and S3, respectively of the ESI section†). The cost of preparing LDH is \$1 per g while that of N4 nanofibers is \$76 per m^2, thereby making it a cost-effective option. However, the filtration output of most of the nanofibers are comparatively higher than the Mg–Al core shell nanofibers. For example, the filtration output of pure PAN/PES nanofiber, reverse osmosis membrane, carbon-based nanofibers, metal oxide-embedded fibers, and cellulose-based nanofibers is 1.13×10^{-4}, 4.86×10^{-5}, 2.78×10^{-4}, 4×10^{-2}, and 4×10^{-5} L m^{-2} h^{-1} Pa^{-1}, respectively. There are previous studies on Mg–Al LDH based PAN and PES uniaxial nanofibers.[63] Uniaxial nanofibers are cheaper with a shorter preparation time in addition to increased filtration output. For example, the filtration output of these two nanofibers are 7.25×10^{-5} and 9.0×10^{-3} L m^{-2} h^{-1} Pa^{-1}, respectively. This is less than the filtration output of core–shell nanofibers (2.8×10^{-6} L m^{-2} h^{-1} Pa^{-1}). However, lead uptake capacities for the uniaxial fibers are much lower than its core and shell counterpart. For example, the lead uptake capacity of Mg–Al LDH based PAN and

Table 4 Comparison of the uptake capacities and cost of various nanofibers

Material	Cost ($ per m^2)	Filtration output (L m^{-2} h^{-1} Pa^{-1})	Lead uptake capacity (mg g^{-1})	Fluoride uptake capacity (mg g^{-1})	Reference
Pure PAN/PES nanofibers	84	1.13×10^{-4}	38	110	4
Reverse osmosis membrane	300	4.86×10^{-5}	Data unavailable	>95% rejection	56
Carbon-based nanofibers	300	2.78×10^{-4}	50–300	10–50	57
Metal oxide-embedded fibers	250	0.04	250	60	58
Cellulose-based nanofibers	150	4×10^{-5}	30	30	59
Mg–Al LDH and PAN based single shell electrospun nanofibers	95	7.25×10^{-5}	120	Data unavailable	63
Mg–Al LDH and PES based single shell electrospun nanofibers	110	0.009	78	Data unavailable	64
PAN–PES/LDH nanofibers	76	2.8×10^{-6}	300	363	Current study

PES uniaxial nanofibers are 120 and 78 mg g^{-1}, respectively, while that for the core–shell counterpart is 300 mg g^{-1}. Unfortunately, there is no data regarding the filtration or removal of fluoride by Mg–Al LDH based uniaxial nanofibers. The significance of using core–shell nanofibers is described in Appendix A of the ESI.† These findings highlight the potential of PAN–PES/LDH nanofibers as a promising material for efficient and economical water purification applications.

4. Conclusion

Coaxial electrospinning was utilized to synthesize polyacrylonitrile–polyethersulfone (PAN–PES) nanofibers impregnated with magnesium–aluminum layered double hydroxide (Mg–Al LDH) filler-based core–shell structures. Nanofibers having a well-defined morphology showed optimum performance at 10 wt% PES/0.7% LDH and 6 wt% PAN. A contact angle of 91° and a porosity of 49% of the optimum performing nanofibers highlighted its hydrophilic and porous nature. Carbon (74%), oxygen (23%), sodium (1.04%), aluminum (1.02%) and magnesium (0.26%) were the primary components of the nanofibers. During thermal analysis, four successive weight losses were observed at 30–200 °C, 200–400 °C, 400–550 °C and 550–620 °C. Sulfone, hydroxyl, ether and nitrile groups were active in the nanofiber structure, resulting in a 66% reduction in lead and 70% reduction in fluoride in batch filtration studies. The uptake capacity for lead in the equilibrium studies was 99 mg g^{-1} at 298 K, 200 mg g^{-1} at 308 K, and 300 mg g^{-1} at 318 K. Similarly, the uptake capacity of fluoride was 100 mg g^{-1} at 298 K, 201 mg g^{-1} at 308 K, and 363 mg g^{-1} at 318 K. The uptake mechanism followed the Langmuir isotherm. The best performing nanofiber had a surface area of 25 m^2 g^{-1}. The most effective removal of pollutants was observed under acidic pH conditions (pH 2) for lead ions and basic pH conditions (pH 11) for fluoride ions. The removal efficiency for lead (1 mg L^{-1}) decreased from 66% to 45% when 100 μg L^{-1} of a coexisting fluoride ion was present in the feed. Similarly, the fluoride removal efficiency dropped significantly from 70% to 12% when 100 μg L^{-1} of a co-existing lead ion was present. The permeate flux was 11.8 L m^{-2} h^{-1} at a lead concentration of 200 μg L^{-1}, while it was 9.3 L m^{-2} h^{-1} at a fluoride concentration of 20 mg L^{-1} under vacuum filtration. The breakthrough time was 12 hours for synthetic solutions (for both lead and fluoride), but decreased to 11 hours for real life feed due to presence of different competing ions.

Nomenclature

Symbols

A	Membrane area, m^2
ARE	Average relative error
C_e	Equilibrium concentration of lead and fluoride in solution, mg L^{-1}
C_f	Concentration of solute in feed, mg L^{-1}
C_0	Feed concentration (lead and fluoride), mg L^{-1}
C_p	Solute concentration in permeate, mg L^{-1}
i	Data points number, dimensionless
J_{w0}	Distilled water flux, m s^{-1}
K	Langmuir isotherm constant, L mg^{-1}
k_f	Freundlich isotherm intensity, mg^{1-n}(L g^{-1})^n
l	Membrane thickness, m
m	Adsorbent's mass (membrane samples) used, g
n	Total number of data points, dimensionless
Q	Amount of permeate collected, L
q_e	Amount of lead and fluoride uptake, mg g^{-1}
$q_{e,meas}$	Empirically determined value of q_e, mg g^{-1}
$q_{e,calc}$	Fitted value of q_e from isotherm, mg g^{-1}
R	Rejection, %
t	Time of agitation for batch adsorption study, h
v	Volume of filtrate recovered for batch adsorption, L
V_m	Maximal capacity of monolayer adsorption (Langmuir isotherm), mg g^{-1}
V	Volume of permeate solution, mL
w_o	Weight of the dry membrane samples, kg
w_l	Weight of the wet membrane samples, kg

Greek symbol

ε	Membrane porosity, dimensionless
ρ_w	Density of water, kg m^{-3}
Δt	Time interval over which permeate samples are taken, h
ΔP	Transmembrane pressure drop, Pa

Abbreviations

BET	Brunauer, Emmett and Teller
DMF	N,N-Dimethylformamide
EDX	Energy dispersive X-ray spectroscopy
FTIR	Fourier transform infrared spectroscopy
HCl	Hydrochloric acid
NaF	Sodium fluoride
NaOH	Sodium hydroxide
PAN	Polyacrylonitrile
PES	Polyethersulfone
SEM	Scanning electron microscopy
SAED	Selected area electron diffraction
TGA	Thermogravimetric analysis
TEM	Transmission electron microscopy
WHO	World Health Organization
XPS	X-ray photoelectron spectroscopy
XRD	X-ray diffraction
RO	Reverse osmosis
CTAB	Cetyltrimethylammonium bromide
LDH	Layered double hydroxides

Data availability

The data supporting this article have been included as part of the ESI.†

Author contributions

Manu Sharma: writing – original draft, visualization, validation, methodology, investigation, and formal analysis; Rushabh Murali: writing–original draft and formal analysis; Karthik K.: validation and formal analysis; Keerthi P.: validation and formal analysis; Somak Chatterjee: writing – review & editing, visualization, validation, supervision, resources, methodology, investigation, formal analysis, funding and conceptualization.

Conflicts of interest

The authors declare that they have no conflict of interest.

Acknowledgements

References

1 A. Mukherjee, D. Saha, C. F. Harvey, R. G. Taylor, K. M. Ahmed and S. N. Bhanja, Groundwater systems of the Indian sub-continent, *J. Hydrol. Reg. Stud.*, 2015, **4**, 1–4.

2 A. K. Taloor, S. Sharma, S. Suryakiran, R. Sharma and M. Sharma, A groundwater contamination and health risk assessment in Indian subcontinent: a geospatial approach, *Curr. Opin. Environ. Sci. Health*, 2024, **7**, 100555–100564.

3 Y. Wang, J. Li, T. Ma, X. Xie, Y. Deng and Y. Gan, Genesis of geogenic contaminated groundwater: As, F and I, *Crit. Rev. Environ. Sci. Technol.*, 2021, **51**, 2895–2933.

4 M. Sharma, K. Karthik, P. Keerthi and S. Chatterjee, Polyacrylonitrile and polyethersulfone based co-axial electrospun nanofibers for fluoride removal from contaminated stream, *Chemosphere*, 2024, **349**, 140837–140847.

5 P. Mushak, A brief early history of lead as an evolving global pollutant and toxicant, *Trace Met. Other Contam. Environ.*, 2011, **10**, 23–39.

6 T. Sanders, Y. Liu, V. Buchner and P. B. Tchounwou, Neurotoxic effects and biomarkers of lead exposure: a review, *Rev. Environ. Health*, 2009, **24**, 15–46.

7 V. Duggal and S. Sharma, Fluoride contamination in drinking water and associated health risk assessment in the Malwa Belt of Punjab, India, *Environ. Adv.*, 2022, **8**, 100242–100250.

8 L. Lv, J. He, M. Wei, D. G. Evans and X. Duan, Factors influencing the removal of fluoride from aqueous solution by calcined Mg–Al–CO$_3$ layered double hydroxides, *J. Hazard. Mater.*, 2006, **133**, 119–128.

9 F. Zhong, P. Wang, Y. He, C. Chen, H. Li, H. Yu and J. Chen, Preparation of stable and superior flux GO/LDH/PDA-based nanofiltration membranes through electrostatic self-assembly for dye purification, *Polym. Adv. Technol.*, 2019, **30**, 1644–1655.

10 E. Oguz, Adsorption of fluoride on gas concrete materials, *J. Hazard. Mater.*, 2005, **117**, 227–233.

11 Z. Amor, B. Bariou, N. Mameri, M. Taky, S. Nicolas and A. Elmidaoui, Fluoride removal from brackish water by electrodialysis, *Desalination*, 2001, **133**, 215–223.

12 C. Castel, M. Schweizer, M. O. Simonnot and M. Sardin, Selective removal of fluoride ions by a two-way ion-exchange cyclic process, *Chem. Eng. Sci.*, 2000, **55**, 3341–3352.

13 N. A. Qasem, R. H. Mohammed and D. U. Lawal, Removal of heavy metal ions from wastewater: a comprehensive and critical review, *npj Clean Water*, 2021, **4**, 1–5.

14 D. H. Reneker and A. L. Yarin, Electrospinning jets and polymer nanofibers, *Polymer*, 2008, **49**, 2387–2425.

15 S. Agrawal, R. Ranjan, B. Lal, A. Rahman, S. P. Singh, T. Selvaratnam and T. Nawaz, Synthesis and water treatment applications of nanofibers by electrospinning, *Processes*, 2021, **9**, 1779–1807.

16 A. Nadaf, A. Gupta, N. Hasan, S. Ahmad, P. Kesharwani and F. J. Ahmad, Recent update on electrospinning and

electrospun nanofibers: current trends and their applications, *RSC Adv.*, 2022, **12**, 23808–23828.

17 V. V. Singh, Green nanotechnology for environmental remediation, in *Sustainable Nanotechnology for Environmental Remediation*, Elsevier, 2022, pp. 31–61.

18 R. H. M. T. Shirazi, T. Mohammadi, A. A. Asadi and M. A. Tofighy, Electrospun nanofiber affinity membranes for water treatment applications: A review, *J. Water Process Eng.*, 2022, **47**, 102795–102817.

19 A. Vazhayil, L. Vazhayal, J. Thomas and N. Thomas, A comprehensive review on the recent developments in transition metal-based electrocatalysts for oxygen evolution reaction, *Appl. Surf. Sci. Adv.*, 2021, **6**, 100184–100224.

20 X. Yang, R. Bai, X. Cao, C. Song and D. Xu, Modification of polyacrylonitrile (PAN) membrane with anchored long and short anionic chains for highly effective anti-fouling performance in oil/water separation, *Sep. Purif. Technol.*, 2023, **316**, 123769–123782.

21 M. J. Mochane, S. I. Magagula, J. S. Sefadi, E. R. Sadiku and T. C. Mokhena, Morphology, thermal stability, and flammability properties of polymer-layered double hydroxide (LDH) nanocomposites: A Review, *Crystals*, 2020, **10**, 612–638.

22 S. Chatterjee and S. De, Adsorptive removal of fluoride by activated alumina doped cellulose acetate phthalate (CAP) mixed matrix membrane, *Sep. Purif. Technol.*, 2014, **125**, 223–238.

23 M. Khitous, Z. Salem and D. Halliche, Removal of phosphate from industrial wastewater using uncalcined MgAl-NO$_3$ layered double hydroxide: batch study and modeling, *Desalin. Water Treat.*, 2016, **57**, 15920–15931.

24 C. Yogeswari, K. M. Hijas, T. S. Girisun and R. Nagalakshmi, Intensity dependent nonlinear absorption switching behavior of electrospun meta-nitroaniline nanofiber, *Opt. Mater.*, 2020, **100**, 109691–109700.

25 M. Yanilmaz, C. Chen and X. Zhang, Fabrication and characterization of SiO$_2$/PVDF composite nanofiber-coated PP nonwoven separators for lithium-ion batteries, *J. Polym. Sci., Part B:Polym. Phys.*, 2013, **51**, 1719–1726.

26 S. H. Othman, S. Abdul Rashid, T. I. Mohd Ghazi and N. Abdullah, Dispersion and stabilization of photocatalytic TiO$_2$ nanoparticles in aqueous suspension for coatings applications, *J. Nanomater.*, 2012, **2012**, 718214–718224.

27 M. Haghgoo, R. Ansari and M. K. Hassanzadeh-Aghdam, The effect of nanoparticle conglomeration on the overall conductivity of nanocomposites, *Int. J. Eng. Sci.*, 2020, **157**, 103392–103416.

28 M. Mohapi, J. S. Sefadi, M. J. Mochane, S. I. Magagula and K. Lebelo, Effect of LDHs and other clays on polymer composite in adsorptive removal of contaminants: a review, *Crystals*, 2020, **10**, 957–996.

29 F. Mokhtari, A. Samadi, A. O. Rashed, X. Li, J. M. Razal, L. Kong, R. J. Varley and S. Zhao, Recent progress in electrospun polyvinylidene fluoride (PVDF)-based nanofibers for sustainable energy and environmental applications, *Prog. Mater. Sci.*, 2024, 101376–101417.

30 X. Yang, T. Kameda, Y. Saito, S. Kumagai and T. Yoshioka, Investigation of the mechanism of Cu(II) removal using Mg-Al layered double hydroxide intercalated with carbonate: Equilibrium and pH studies and solid-state analyses, *Inorg. Chem. Commun.*, 2021, **132**, 108839–108844.

31 M. A. Teixeira, A. B. Mageste, A. Dias, L. S. Virtuoso and K. P. Siqueira, Layered double hydroxides for remediation of industrial wastewater containing manganese and fluoride, *J. Cleaner Prod.*, 2018, **171**, 275–284.

32 G. B. Varadwaj, O. A. Oyetade, S. Rana, B. S. Martincigh, S. B. Jonnalagadda and V. O. Nyamori, Facile synthesis of three-dimensional Mg–Al layered double hydroxide/ partially reduced graphene oxide nanocomposites for the effective removal of Pb^{2+} from aqueous solution, *ACS Appl. Mater. Interfaces*, 2017, **9**, 17290–17305.

33 M. T. Hossain, S. Khandaker, M. M. Bashar, A. Islam, M. Ahmed, R. Akter, A. K. Alsukaibi, M. M. Hasan, H. M. Alshammari, T. Kuba and M. R. Awual, Simultaneous toxic Cd(II) and Pb(II) encapsulation from contaminated water using Mg/Al-LDH composite materials, *J. Mol. Liq.*, 2022, **368**, 120810–120811.

34 X. Li, S. Chen, Z. Xia, L. Li and W. Yuan, High performance of boehmite/polyacrylonitrile composite nanofiber membrane for polymer lithium-ion battery, *RSC Adv.*, 2020, **10**, 27492–27501.

35 N. Kizildag, Smart composite nanofiber mats with thermal management functionality, *Sci. Rep.*, 2021, **11**, 4256–4272.

36 R. A. Ismail, Development of novel functionalized polydopamine-enabled mixed matrix membranes for wastewater treatment application, PhD thesis, Khalifa University of Science, 2021.

37 S. Ayyaru and Y. H. Ahn, Fabrication and separation performance of polyethersulfone/sulfonated TiO$_2$ (PES–STiO$_2$) ultrafiltration membranes for fouling mitigation, *J. Ind. Eng. Chem.*, 2018, **67**, 199–207.

38 L. Hongtao, L. Shuxia, Z. Hua, Q. Yanling, Y. Daqiang, Z. Jianfu and Z. Zhiliang, Comparative study on synchronous adsorption of arsenate and fluoride in aqueous solution onto MgAlFe-LDHs with different intercalating anions, *RSC Adv.*, 2018, **8**, 33301–33313.

39 S. Z. Ahmad, W. N. Salleh, A. F. Ismail, N. Yusof, M. Z. Yusop and F. Aziz, Adsorptive removal of heavy metal ions using graphene-based nanomaterials: Toxicity, roles of functional groups and mechanisms, *Chemosphere*, 2020, **248**, 126008–126024.

40 J. Singh, P. Singh and A. Singh, Fluoride ions *vs.* removal technologies: A study, *Arabian J. Chem.*, 2016, **9**, 815–824.

41 B. M. Thamer, A. Aldalbahi, A. M. Moydeen, A. M. Al-Enizi, H. El-Hamshary and M. H. El-Newehy, Fabrication of functionalized electrospun carbon nanofibers for enhancing lead-ion adsorption from aqueous solutions, *Sci. Rep.*, 2019, **9**, 19467–19482.

42 E. G. Söğüt and M. Gülcan, Adsorption: basics, properties, and classification, in *Adsorption through Advanced Nanoscale Materials*, Elsevier, 2023, pp. 3–21.

43 A. Rathnayake, O. Hettithanthri, S. Sandanayake, K. Mahatantila, A. U. Rajapaksha and M. Vithanage,

Essence of hydroxyapatite in defluoridation of drinking water: A review, *Environ. Pollut.*, 2022, **311**, 119882–119894.

44 A. Elhalil, S. Qourzal, F. Z. Mahjoubi, R. Elmoubarki, M. Farnane, H. Tounsadi, M. Sadiq, M. Abdennouri and N. Barka, Defluoridation of groundwater by calcined Mg/Al layered double hydroxide, *Emerging Contam.*, 2016, **2**, 42–48.

45 X. Feng, R. Long, L. Wang, C. Liu, Z. Bai and X. Liu, A review on heavy metal ions adsorption from water by layered double hydroxide and its composites, *Sep. Purif. Technol.*, 2022, **284**, 120099–120145.

46 J. Wei, W. Wang, L. Ge, J. Lu, P. Hong, Y. Li, Y. Li, C. Xie, Z. Wu, J. He and L. Kong, Nanoconfinement regulation of La-Mg LDH/$Ti_3C_2T_x$ (T = O, OH) for effective removal of fluoride: Membrane fabrication and mechanism revelation, *Chem. Eng. J.*, 2024, **493**, 152779.

47 Y. Li, S. Wang, X. F. Ouyang, Z. Dang and H. Yin, Acetate anions intercalated Fe/Mg-layered double hydroxides modified biochar for efficient adsorption of anionic and cationic heavy metal ions from polluted water, *Chemosphere*, 2024, **362**, 142652–142665.

48 B. A. Al-Rashdi, D. J. Johnson and N. Hilal, Removal of heavy metal ions by nanofiltration, *Desalination*, 2013, **315**, 2–17.

49 B. Kim, G. Gwak and S. Hong, Review on methodology for determining forward osmosis (FO) membrane characteristics: Water permeability (A), solute permeability (B), and structural parameter (S), *Desalination*, 2017, **422**, 5–16.

50 Y. Han, Z. Xu and C. Gao, Ultrathin graphene nanofiltration membrane for water purification, *Adv. Funct. Mater.*, 2013, **23**, 3693–3700.

51 J. Qian, H. Zhan, Z. Chen and H. Ye, Experimental study of solute transport under non-Darcian flow in a single fracture, *J. Hydrol.*, 2011, **399**, 246–254.

52 P. Bhunia, S. Chatterjee, P. Rudra and S. De, Chelating polyacrylonitrile beads for removal of lead and cadmium from wastewater, *Sep. Purif. Technol.*, 2018, **193**, 202–213.

53 F. A. Alnasrawi, A. A. Mohammed, T. J. Al-Musawi and N. M. Hussein, The efficient elimination of lead ions from aqueous solution using MgCuAl-layered double hydroxides@ montmorillonite composite: A kinetic, isotherm and statistical analysis, *Results Surf. Interfaces*, 2024, **16**, 100260–100275.

54 Y. Wang, J. Li, L. Xu, D. Wu, Q. Li, Y. Ai, W. Liu, D. Li, Y. Zhou, B. Zhang and N. Guo, EDTA functionalized Mg/Al hydroxides modified biochar for Pb(II) and Cd(II) removal: Adsorption performance and mechanism, *Sep. Purif. Technol.*, 2024, **335**, 126199–126209.

55 Y. Su, Y. Wen, W. Yang, X. Zhang, M. Xia, N. Zhou, Y. Xiong and Z. Zhou, The mechanism transformation of ramie biochar's cadmium adsorption by aging, *Bioresour. Technol.*, 2021, **330**, 124947–124953.

56 M. Hafiz, A. H. Hawari, R. Alfahel, M. K. Hassan and A. Altaee, Comparison of nanofiltration with reverse osmosis in reclaiming tertiary treated municipal wastewater for irrigation purposes, *Membranes*, 2021, **11**, 32–45.

57 R. Yadav, O. Zabihi, S. Fakhrhoseini, H. A. Nazarloo, A. Kiziltas, P. Blanchard and M. Naebe, Lignin derived carbon fiber and nanofiber: Manufacturing and applications, *Composites, Part B*, 2023, **255**, 110613–110641.

58 M. Islam, C. Dolle, A. Sadaf, P. G. Weidler, B. Sharma, Y. M. Eggeler, D. Mager and J. G. Korvink, Electrospun carbon nanofibre-assisted patterning of metal oxide nanostructures, *Microsyst. Nanoeng.*, 2022, **8**, 71–85.

59 A. Serra, I. González, H. Oliver-Ortega, Q. Tarrès, M. Delgado-Aguilar and P. Mutjé, Reducing the amount of catalyst in TEMPO-oxidized cellulose nanofibers: Effect on properties and cost, *Polymers*, 2017, **9**, 557–571.

60 E. M. Abd El-Monaem, H. M. Elshishini, S. S. Bakr, H. G. El-Aqapa, M. Hosny, G. Andaluri, G. M. El-Subruiti, A. M. Omer and A. S. Eltaweil, A comprehensive review on LDH-based catalysts to activate persulfates for the degradation of organic pollutants, *npj Clean Water*, 2023, **6**, 34–58.

61 R. Rojas, D. Bedoya, C. Vasti and C. Giacomelli, LDH nanoparticles: synthesis, size control and applications in nanomedicine, in *Layered Double Hydroxides (LDHs): Synthesis, Characterization and Applications*, 2015, pp. 101–120.

62 S. Velu, G. Arthanareeswaran and H. Lade, Removal of organic and inorganic substances from industry wastewaters using modified aluminosilicate-based polyethersulfone ultrafiltration membranes, *Environ. Prog. Sustainable Energy*, 2017, **36**, 1612–1620.

63 H. Chen, J. Lin, N. Zhang, L. Chen, S. Zhong, Y. Wang, W. Zhang and Q. Ling, Preparation of MgAl-EDTA-LDH based electrospun nanofiber membrane and its adsorption properties of copper(II) from wastewater, *J. Hazard. Mater.*, 2018, **345**, 1–9.

64 M. Sajid, S. M. Jillani, N. Baig and K. Alhooshani, Layered double hydroxide-modified membranes for water treatment: Recent advances and prospects, *Chemosphere*, 2022, **287**, 132140–132155.